Journal of Materials Chemistry A

ROYAL SOCIETY OF CHEMISTRY

PAPER

View Article Online
View Journal | View Issue

Cite this: *J. Mater. Chem. A*, 2025, **13**, 21929

Molecular engineering of ethereal electrolyte for ultrastable Si-based high voltage full cells†

Xianyang Wu,‡[a] Chi-Cheung Su, ‡[a] Xinlin Li,[a] Jiayi Xu,[a] Khalil Amine, [a] Dezhen Wu,[a] Tianyi Li, [b] Zhenzhen Yang *[a] and Brian J. Ingram [a]

Received 6th March 2025
Accepted 3rd June 2025

DOI: 10.1039/d5ta01872b

rsc.li/materials-a

The successful application of Si-based high-energy Li-ion batteries (LIBs) depends on our ability to tailor electrolyte properties to achieve long-term stability and reliable performance. In this work, we demonstrate our rationale for the molecular design of ethereal solvents to address low anodic stability issues and produce a highly electrochemically stable electrolyte for Si||$LiNi_{0.8}Mn_{0.1}Co_{0.1}O_2$ (NMC811) high-energy full cells. Unlike the trimethylsilyl group, the trifluoromethyl ($-CF_3$) group exerts a very strong electron-withdrawing effect on the glycol ether backbone, reducing the highest occupied molecular orbital (HOMO) energy level of the fluorinated glycol ether (FGE) and significantly enhancing its oxidation potential. The FGE-based electrolyte enables stable cycling of Si||NMC811 full cells, delivering high specific capacity (900 mA h g^{-1}) and coulombic efficiency (>99.78%) over extended (500) cycles. The improved electrochemical performance originates from the terminal fluorination of the diglyme backbone, which strengthens anion coordination in the solvation structure, leading to the preferential reduction of the FSI anion and the formation of robust solid electrolyte interphases (SEIs) on the Si surface. Through molecular engineering of ethereal solvents, we have discovered a promising candidate for a next-generation stable electrolyte, paving the way for the design of practical and commercially viable Si batteries.

1. Introduction

Since their first commercialization in the 1990s, lithium-ion batteries (LIBs) have dominated the global market for rechargeable applications[1,2] Graphite has maintained its position as the primary anode material for commercialized LIBs.[3–5] However, the increasing need for higher energy density in various devices is driving the search for novel anode materials with higher specific capacities.[6] Silicon (Si) is one such material, known for its abundance, non-toxicity, and high specific capacity (3579 mA h g^{-1} when charged to $Li_{15}Si_4$ at room temperature).[7,8] It has garnered significant interest and is emerging as a promising replacement for graphite anodes in LIBs. However, recent studies indicate its mass application in LIBs has been greatly hindered by following challenges.[8–11] Firstly, lithiated Si exhibits high chemical reactivity with electrolyte once in contact and leads to the continued decomposition of electrolyte and formation of irreversible reaction products during cycling.[12] Secondly, Si anodes undergo large volume expansions/shrinkage during the charging/discharging process (~300% volume expansion during charging).[8] This mechanical stress breakdowns the SEI layer on Si anode and the electrode structure.[13] Moreover, the inherent instability of Si as an electrode material, particularly in its amorphous or nanostructured forms, can exacerbate degradation mechanisms and limit the long-term stability. All these factors result in increased impedance and reduced capacity retention over time in both cycling performance and calendar performance.

Correspondingly, various strategies have been explored by the community to mitigate these degradation effects. These strategies include doping of Cu/Se into Si anodes, utilization of binder with improved mechanistic properties to enhance bonding between binder and Si anode materials, development of novel electrolyte systems, as well as the optimization of silicon anode morphology. Among these approaches, development of novel electrolyte systems with enhanced stability towards Si anode is recognized as the most effective solution. Recently, ethereal based electrolytes have been found to form better solid electrolyte interphases (SEIs) and thus improve their electrochemical performance for LIBs using Si anode.[14] For example, the research community has explored electrolytes based on ethereal solvents such as dimethoxyethane (DME), as alternatives to conventional electrolytes due to their promising capability to form a robust SEI on Si anodes. These new electrolytes enhances the long-term and calendar aging performance of Si||Li half cells.[14] While ethereal solvents have

[a]*Chemical Sciences and Engineering Division, Argonne National Laboratory, Lemont, Illinois 60439, USA. E-mail: yangzhzh@anl.gov*

[b]*X-Ray Science Division, Argonne National Laboratory, Lemont, Illinois 60439, USA*

† Electronic supplementary information (ESI) available. See DOI: https://doi.org/10.1039/d5ta01872b

‡ Xianyang Wu and Chi-Cheung Su contributed equally to this work.

demonstrated excellent reductive stability with silicon anodes, they encounter challenges with oxidative stability when paired with high-voltage and higher energy cathodes.[15,16] To address this critical issue, *via* molecular engineering, we investigated the impact of functionalization on regular ethers. Our research revealed that fluorinating the glycol ether provided the most significant enhancement in cell performance.

In this study, we systematically examined the influence of several innovative electrolyte systems, employing lithium bis(-fluorosulfonyl)imide (LiFSI) salt and a variety of ethereal solvents, on high-voltage silicon-based LIBs. The ethereal solvents studied included commercially available diglyme (DG) and dimethoxyethane (DME), as well as synthetic solvents 2,2-dimethyl-3,6,9,12-tetraoxa-2-silatridecane (1NM3) and 1,1,1-trifluoro-2-(2-(2-(2,2,2-trifluoroethoxy)ethoxy)ethoxy)ethane (FDG). We initially compared the highest occupied molecular orbital (HOMO) and lowest unoccupied molecular orbital (LUMO) levels of the molecules using density functional theory (DFT) calculations. The results indicated that FDG possesses significantly higher anodic stability than the other three solvents. We then evaluated the electrochemical properties and performances of these electrolytes on Li||Al, Li||Si half cells, and Si||$LiNi_{0.8}Mn_{0.1}Co_{0.1}O_2$ (NMC811) full cells. While the full cell using 1NM3 electrolyte exhibited improved long-term cycling performance compared to the cells using DME or DG electrolytes, possibly due to the slightly enhanced oxidative stability of 1NM3,[17] the cell utilizing FDG-based electrolytes demonstrated significantly better performance. For the superior performance of the FDG electrolytes, on the cathode side, our interfacial analysis of the electrodes using depth-profiling X-ray photoelectron spectroscopy (XPS) suggested the enhanced oxidative stability of FDG towards the high-voltage NMC811, resulting in improved electrochemical performances. On the Si anode side, it was attributed to their significantly higher aggregate level, as evidenced by Fourier Transform Infrared Spectroscopy (FTIR) studies. This higher aggregate level led to the preferential reduction of LiFSI and the formation of a robust SEI layer.

2 Results and discussions

2.1 Molecular design of ethereal solvents

Functional electrolytes, which consist of LiFSI salt dissolved in regular ethers like DME or DG, have shown significant enhancements in electrochemical performance on Si anodes compared to conventional carbonate-based electrolytes.[18,19] However, their application on high-voltage NMC cathodes is limited due to their relatively low oxidation potential. One potential solution is the incorporation of functional groups that can modify the redox potential of the ether molecule. Trimethylsilyl and fluorinated alkyl groups, are well known to improve oxidation stability of regular ethers and have been successfully utilized in high-voltage LIBs.[20] In this context, 1NM3 and FDG have been selected as the functionalized ethereal solvents for developing the new electrolyte system, and their chemical structures are illustrated in Fig. 1a.

To assess the impact of functional groups on the ether backbone on the electrochemical windows, we conducted DFT calculations to compare the HOMO and LUMO levels of all four molecules, with the results summarized in Fig. 1b. The LUMO and HOMO levels of solvents are well recognized as common descriptors for electrolyte stability: the LUMO level correlates with the reduction of the liquid electrolyte at the anode side, while the HOMO energy level correlates with the oxidation of the liquid electrolyte at the cathode side.[21,22] Among the studied solvent molecules, DME and DG exhibit larger HOMO–LUMO gap than the functionalized molecules 1NM3 and FDG, with the gaps of 22.886 eV (DME), 22.289 eV (DG), 20.598 eV (1NM3) and 21.636 eV (FDG), respectively. Upon the addition of a trimethylsilyl group, the calculated HOMO level of 1NM3 slightly increases to −8.255 eV, compared to the similar HOMO levels of DME and DG at −8.987 eV and −8.998 eV, respectively. In contrast, the LUMO level of 1NM3 decreases significantly. This result suggests that the trimethylsilyl substitution may not be suitable due to its increased reactivity both as an electron donor and acceptor. Ideally, the functionalization of the ether backbone should increase the LUMO level while decreasing the HOMO level, thereby widening the electrochemical windows.[23,24] However, the decrease in the HOMO level through functionalization of a molecule will inevitably lead to a decrease in the LUMO level due to the strong electron-withdrawing effect of the added functional group.[24] This is exemplified by the calculated results of FDG, which show a decrease in the HOMO level (−9.129 eV) compared to DME (−8.987 eV), attributed to the attachment of the strong electron-withdrawing trifluoromethyl group. FDG shows more compatible with the high-voltage NMC811 cathode, but its lower LUMO may indicate it is more prone to electron uptake and thus more reactive in reductive processes compared to the regular ethers. However, this does not necessarily imply that FDG is unstable towards the Si anode, as the stability at the anode side heavily depends on the quality of the SEI, which serves as a kinetic barrier between lithiated Si and electrolyte components.[11] This is also why fluoroethylene carbonate (FEC) is considered a better solvent for the Si anode than ethylene carbonate (EC), despite having a lower LUMO level.[25–27] Nevertheless, due to the enhanced oxidation stability and potentially reduced lithium solvating ability of FDG, it is considered as a promising solvent for the electrolyte used in high-voltage Si||NMC full cells. And for the synthesized FDG solvent, the ^{1}H and ^{19}F nuclear magnetic resonance (NMR) spectra, shown in Fig. 1c and d, confirm the successful synthesis with no detectable impurities.

2.2 The electrochemical properties of ethereal electrolytes

To better understand the structure–activity relationships between the ether solvents and their electrochemical activity, we initially measured the ionic conductivity of the ethereal electrolytes from 20 °C to 60 °C, with the results presented in Fig. 2. Compared to their regular ether counterparts (DME and DG), although possessing much lower salt concentration, electrolytes based on 1NM3 and FDG solvents exhibit relatively lower ionic conductivity at the given temperature, likely due to their increased viscosity resulting from elongated chain lengths and fluorination.[28] This hypothesis is supported by the

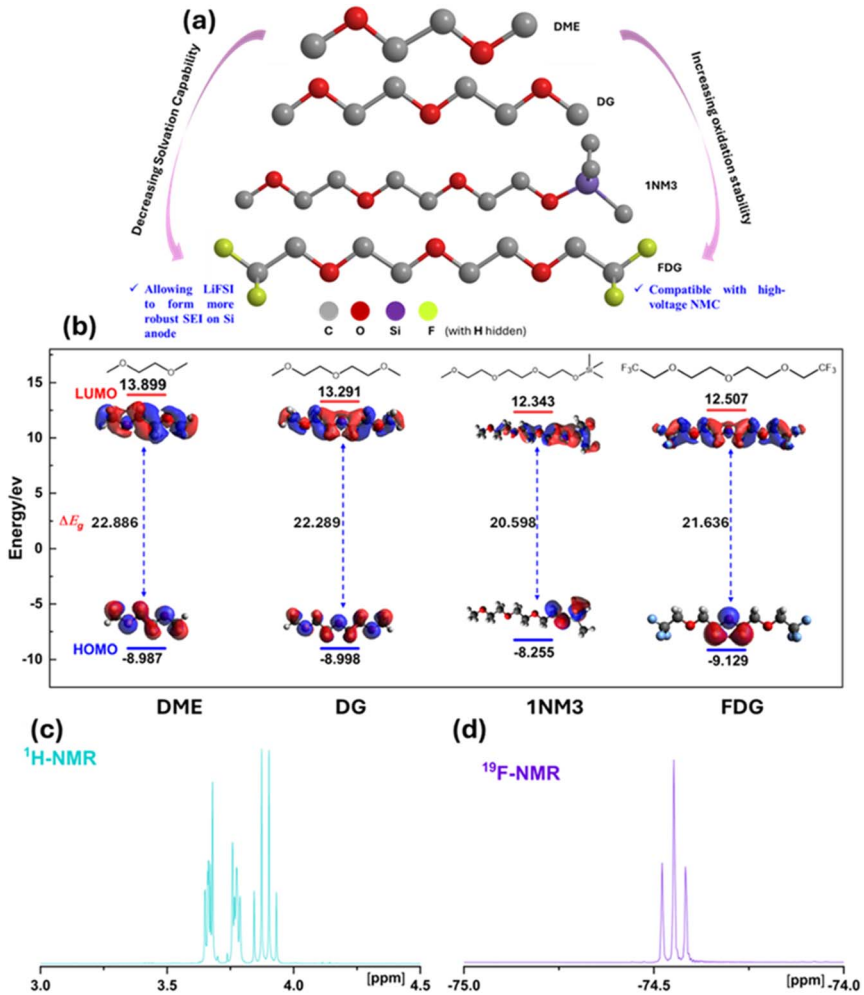

Fig. 1 The rationale behind the utilization of the DME, DG, 1NM3 and FDG ethereal solvent for NMC811||Si full cells (a) the chemical structures of the 4 solvents probed in this study; (b) the HOMO and LUMO levels of four solvent molecules obtained *via* DFT calculations with solvation effect considered; (c) the ^{1}H-NMR of synthesized FDG solvent; (d) the ^{19}F-NMR of synthesized FDG solvent.

activation energies (E_a) for the Arrhenius behavior observed between the ionic conductivity and temperature, where the 1NM3-and FDG-based electrolyte display higher E_a values than the DME- and DG-based electrolyte, with corresponding E_a values of 0.207 eV (DME), 0.165 eV (DG), 0.215 eV (1NM3), 0.271 eV (FDG).[29] Additionally, the inclusion of the strong electron-withdrawing fluorinated alkyl group in FDG diminishes its lithium solvating ability, thereby reducing its capacity

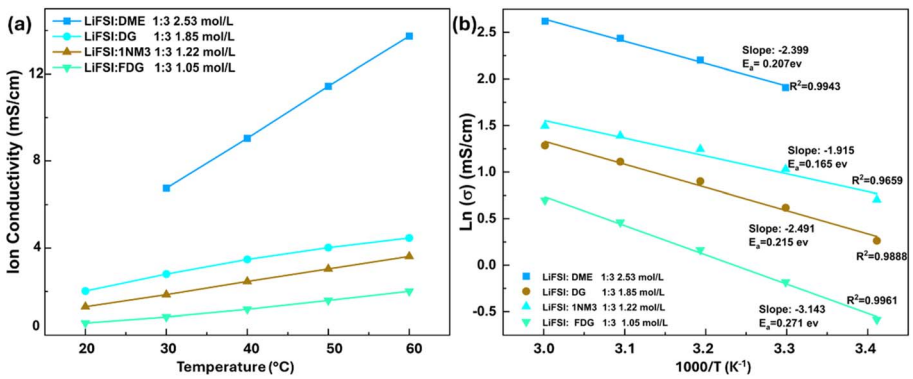

Fig. 2 The (a) ion conductivity of probed electrolytes (for the LiFSI : DME 1 : 3 (molar : molar) electrolyte, the ion conductivity at 20 °C is missing because the electrolyte got frozen under 20 °C, as shown in Fig. S4†); (b) activation energies obtained from the Arrhenius equation for the tested electrolyte systems.

to dissociate LiFSI salt and further decrease the ionic conductivity of the FDG electrolyte. Meanwhile, it is important to note that the conductivities of both 1NM3- and FDG-based electrolytes remain within the same magnitude as that of the DG-based electrolyte, retaining stability for charging Si||NMC811 full cells at normal rates (<0.5C).

In addition to ionic conductivity, the solvation structure of a liquid electrolyte also plays a crucial role in determining the chemistry at the electrode/electrolyte interfaces.[30,31] As the concentration of lithium salt increases, there is a decrease in the relative ratio of solvent-separated ion pairs (SSIPs), accompanied by an increase in both contact ion pairs (CIPs) and cation–anion aggregates (AGGs). [32,33] This phenomenon can be qualitatively probed using FTIR. Fig. 3a and b display the FTIR spectra of LiFSI-DME electrolytes with varying salt-to-solvent ratios, illustrating the evolution of solvation structure with increasing salt concentration. Initially, there is a LiFSI absorption peak at around 572 cm^{-1} for the dilute electrolyte (LiFSI : DME in 1 : 8 molar ratio). Upon the increase in LiFSI ratio from 1 : 8 to 1 : 1, a peak at around 575 cm^{-1} emerged and gradually increased in its intensity, which corresponds to the vibration of LiFSI in AGGs.[34] This process clearly indicated the transition of LiFSI solvation state from dominantly SSIPs at low concentration to majorly AGGs at high salt concentration.

Subsequently, we evaluated the solvation structures of five different electrolytes using FTIR, and the results are displayed in Fig. 3c. For the FDG-based electrolytes, the C–F stretching from the fluoroalkyl group is clearly seen from the peak at ~1275 cm^{-1}. For the FSI anion, although several absorption peaks from the FSI anion overlapped with peaks from the solvents, we were still able to identify distinctive absorption peaks at approximately 570 cm^{-1}, corresponding to the asymmetric bending of O═S═O from the FSI anion, and at 860 cm^{-1}, corresponding to the asymmetric stretching of S–N–S in the FSI anion.[34–36]

It is evident that the FDG-based electrolytes behave significantly differently from those based on DME, DG, and 1NM3. As depicted in Fig. 3c and d, the relative ratio of the 575 cm^{-1} peak to the 572 cm^{-1} peak for FDG-based electrolytes is significantly higher than that of the other electrolytes, indicating a larger percentage of AGGs present in FDG-based electrolytes, even at a relatively low concentration of LiFSI (LiFSI : FDG molar ratio 1 : 8 corresponds to 0.55 mol L^{-1} LiFSI in FDG and LiFSI : FDG 1 : 3 molar ratio corresponds to 1.05 mol L^{-1} LiFSI in FDG). The evolution of solvation structure is also verified *via* ^{19}F NMR. As shown in Fig. S5,† the FDG13 electrolyte shows lowest chemical shift to ~51.57 ppm, indicating the presence of more AGGs. This phenomenon can be explained by the introduction of the

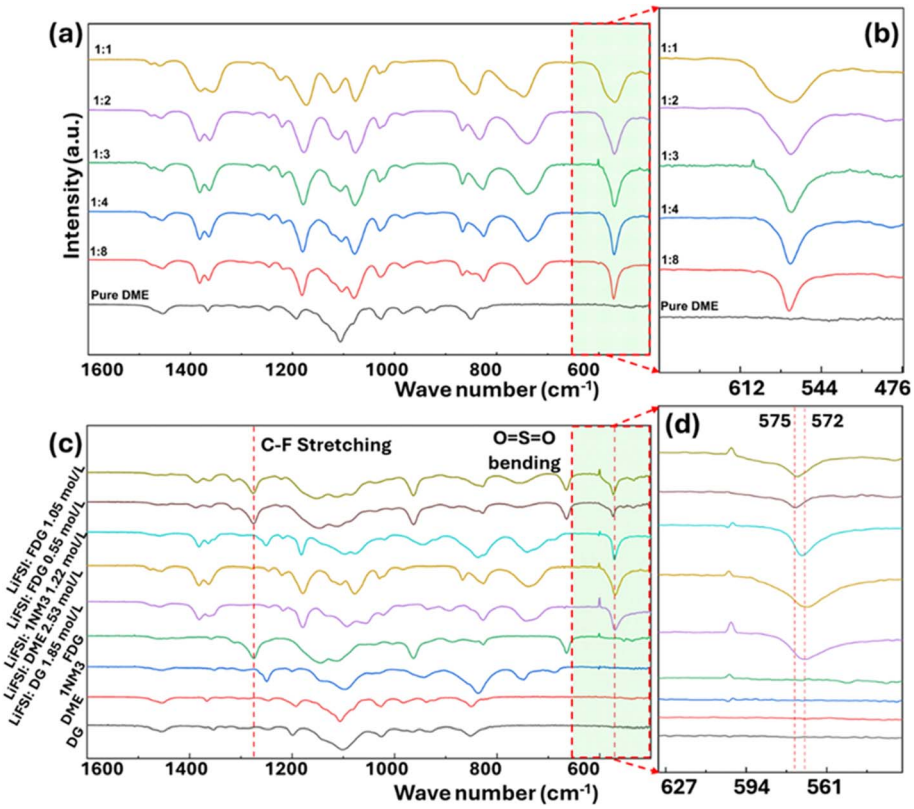

Fig. 3 The evolution of solvation structure for tested electrolytes with increasing LiFSI salt concentration (a) the overall spectrum of LiFSI : DME electrolytes with increasing LiFSI concentration from 1 : 8 to 1 : 1 (molar ratio) between 1600 and 500 cm^{-1} and (b) the detailed spectrum from 680 to 476 cm^{-1} exhibiting the increasing content of AGGs formed with increasing LiFSI concentration; (c) the overall spectra from 1600–500 cm^{-1} for electrolytes from different solvents; also note that two concentrations from FDG were compared to reflect salt effect (d) the absorption modes showing evolution of FSI anions within these electrolytes.

fluoroalkyl group in FDG, which has a strong electron-withdrawing effect that significantly reduces the electron density on the lone pair of electrons of the O atom, leading to its lower polarization and weaker solvation capability. Consequently, the solvation state of the LiFSI-FDG electrolytes is dominated by AGGs, making it easier for FSI anions to participate in the reduction process at Si anodes. Given the capability of FSI anions in forming a robust SEI on Si anodes, it is expected that the SEI formed on the Si anode by FDG-based electrolytes is more stable than the SEI initiated by the other electrolytes.[18,19]

2.3 Electrochemical performance

To effectively use LiFSI-based electrolytes with NMC cathodes, it is crucial to prevent the corrosion of the aluminum (Al) current collector at voltages exceeding 4 V *vs.* Li/Li^+.[37] Therefore, we conducted potentiostatic experiments on Li||Al half-cells using DME- and FDG-based electrolytes to study the corrosion behavior of the Al current collector. Unlike the LiFSI-DME electrolyte at a normal concentration (~1 M), which is highly susceptible to Al corrosion, the relatively concentrated 2.5 M LiFSI-DME electrolyte resisted corrosion until 4.7 V *vs.* Li/Li^+, as illustrated in Fig. S6a.†[38] Moreover, the normal concentration (1 M) LiFSI-FDG electrolyte demonstrated the ability to mitigate Al corrosion even at 4.8 V *vs.* Li/Li^+ (Fig. S6b†). The superior aluminum corrosion resistance of the LiFSI-FDG electrolyte compared to the LiFSI-DME electrolyte is further demonstrated through SEM images. As shown in Fig. S7,† the Al foil held at 4.8 V *vs.* Li/Li^+ for 10 hours in the LiFSI-FDG electrolyte exhibits almost no signs of corrosion, maintaining its pristine appearance. In contrast, significant voids and pitting due to corrosion

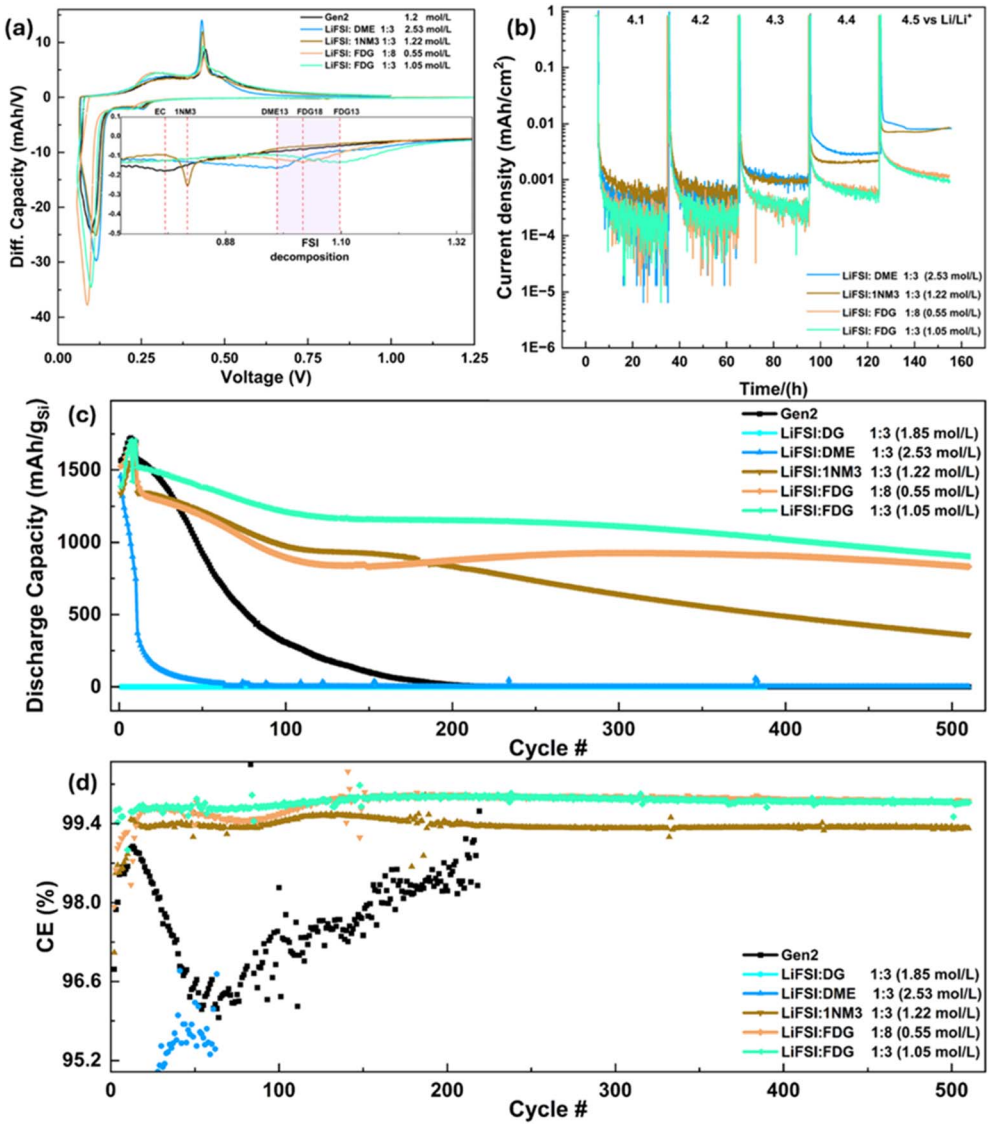

Fig. 4 The electrochemical results for tested electrolyte systems: (a) the dQ/dV curves for these 5 electrolyte systems; (b) the voltage holding results on NMC811||Li half cells between 4.1–4.5 V *vs.* Li/Li^+; (c) the long-term cycling results for NMC811||Si full cells between 3.0–4.3 V *vs.* Li/Li^+ at C/3, the specific capacity is calculated based on the mass of Si; (d) the coulombic efficiencies of the tested electrolytes during the long-term cycling.

are clearly visible on the Al foil exposed to the LiFSI-DME electrolyte under the same conditions. This outstanding compatibility between the FDG electrolyte and the Al current collector is likely due to the reduced solvating ability of the FDG solvent, making the dissolution of aluminum significantly more challenging.

The reduction behavior of DME, FDG, and 1NM3 electrolyte systems was further evaluated using the differential capacity (dQ/dV) profiles of Li||Si half-cells, which were then compared with the profile of the conventional carbonate Gen 2 electrolyte (1.2 M $LiPF_6$ in EC/EMC with the weight ratio of 3/7). As depicted in Fig. 4a, a small distinctive peak around 0.78 V *vs.* Li/Li^+ for the Gen 2 electrolyte indicates the EC reduction process. In contrast, for all LiFSI-containing electrolytes, the reduction process began at around 1 V *vs.* Li/Li^+, corresponding to the reduction of the LiFSI salt in forming the SEI.[39] Notably, for the 1NM3-based electrolyte, an anodic current peak is also observed at ~0.82 V *vs.* Li/Li^+, which is believed to be the reduction of the 1NM3 solvent.[17]

Although the oxidative stability of these ethereal solvents has been probed *via* DFT calculations, to further confirm the oxidative stability of these ethereal electrolyte systems, potentiostatic hold experiments on NMC811||Li half cells from initial 4.1 V to highest 4.5 V *vs.* Li/Li^+ were also implemented. And the results were summarized in Fig. 4b. When the holding voltage is within 4.2 V *vs.* Li/Li^+, the four electrolytes (DME13, 1NM313, FDG18 and FDG13) all show similar current density. As the holding voltage increases to 4.3 V, corresponding current density increases and the current densities of DME13, 1NM313 start to increase; when it increases to 4.4 V, it is seen that all current densities of these 4 electrolytes increase with the DME13 electrolyte showing highest current density and the FDG13 electrolyte the smallest. From the voltage holding results, we can infer that for the oxidative stability of these 4 electrolytes, the FDG13 and the FDG18 have higher stability than the DME13 and the 1NM313, with the DME13 the least stable within these 4 electrolytes.

Fig. 4c and d illustrated the long-term cycling performance of Si||NMC811 full cells using Gen2 and various ethereal electrolytes. Noting that the specific capacity in Fig. 4 was calculated according to the weight of active Si, while the specific capacity calculated by the weight of NMC811 is displayed in Fig. S8a.† The DG13 electrolyte exhibits almost no capacity, possibly due to the polymerization of DG triggered by the acidic environment, leading to the loss of Li transport capability upon cycling.[40] As shown in Fig. S9,† this polymerization behavior of DG13 electrolyte is also verified after stirring it for several hours within glovebox. Unsatisfactory cycling performance was also observed with the cell employing the other regular ether, DME, as an electrolyte solvent, which displayed very fast capacity degradation with almost all capacity gone after only 50 cycles. Clearly, the cells using regular ethers as electrolyte solvents demonstrated inferior performance even when compared to the cell employing conventional Gen2 electrolyte, which lost all its capacity after a significantly longer 200 cycles. Considering the results from potentiostatic hold experiments and their good performance within Si||Li half cells, it is reasonable to attribute this fast capacity degradation to the oxidative instability of regular ether solvents. The cells utilizing the 1NM313, FDG18, and FDG13 electrolytes demonstrated significant improvements compared to the Gen2 baseline cell. Specifically, the 1NM313 cell retained a capacity of 360 mA h g^{-1} for the Si anode after 500 cycles, while the FDG13 cell (1.05 M) achieved a specific capacity of approximately 900 mA h g^{-1} with the lowest fading rate (Fig. S8b†) after the same number of cycles. Similarly, the FDG18 cell (0.55 M) retained 832 mA h g^{-1}, further confirming the trend that increasing salt concentration enhances capacity retention by stabilizing the electrolyte system. Additionally, the overall coulombic efficiencies (CEs) of the cells throughout the 500 cycles were consistent with their long-term cycling performance. The DME13 cell exhibited the lowest CEs, below 96% within the initial 50 cycles, while the Gen2 cell possessed a CE ranging from 95.7% to 98.6%. The 1NM313 cell showed a stable CE of around 99.33%, and the FDG18 and FDG13 cells presented the highest CEs at 99.78%. The greatly enhanced CEs of the 1NM313, FDG18, and FDG13 cells are likely due to the formation of more robust SEIs on Si anodes and the enhanced oxidative stability of the solvents. It is also noteworthy that the LiFSI concentrations of 1NM313 and FDG13 electrolytes are 1.22 M and 1.05 M, respectively, which represent a normal salt concentration for an electrolyte (Table 1). In contrast, the LiFSI concentration of DME13 electrolyte is 2.5 M, which is significantly more concentrated than the 1NM313 and FDG electrolytes. The superior performance of FDG electrolytes with higher capacity and lower fade rate, even at a relatively low concentration (0.55–1.55 M), clearly demonstrates their potential application in Si||NMC full cells. While 500 cycles is a significant milestone for demonstrating stability in laboratory settings, it may be feasible to indicate ultrastability for an even longer lifetime as capacity decay slows down in the later stages (*i.e.* >100 cycle), as the fade rate analysis shown in Fig. S8b.† However, long-term cycling tests over thousands of cycles, coupled with real-world conditions such as varying temperatures and current rates, are essential to fully validate the robustness and practicality of this electrolyte system.

2.4 Characterization on the morphology and interphases

To better understand the reasons behind their different long-term cycling performance, the morphology evolutions of

Table 1 Electrolytes tested in this study and their detailed formulations[a]

Electrolyte ID	Electrolyte formula	Salt concentration (mol L^{-1})
Gen2	1.2 M $LiPF_6$ in EC/EMC (3 : 7 wt/wt)	1.2
DME13	LiFSI : DME 1 : 3 mol/mol	2.53
DG13	LiFSI : DG 1 : 3 mol/mol	1.85
1NM313	LiFSI : 1NM3 1 : 3 mol/mol	1.22
FDG18	LiFSI : FDG 1 : 8 mol/mol	0.55
FDG13	LiFSI : FDG 1 : 3 mol/mol	1.05

[a] Note: here the w/w stands for weight ratio and the m/m stands for molar ratio.

NMC811 cathodes and Si anodes from initial formation step through 500C/3 cycles were imaged by SEM. As shown in Fig. 5, for the NMC811 cathodes, typical cracks between primary NMC811 were observed and no significant difference is observed for NMC811 using different electrolytes, either from the calendar process or from the volume expansion/shrinkage during charging/discharging process. For Si anodes, cracking due to strong volume expansion/shrinkage during charging/discharging is commonly observed.[41] And the morphology of electrodes experiencing formation and long-term cycling from the four electrolytes were compared. As shown in Fig. 5i–p, compared to the pristine Si anode, all the Si anodes show significant cracks even after the formation process and there is no significant evolution of these cracks after 500 cycles. For the Si anodes from Gen2 sample, the bonding between Si and copper (Cu) current collector experienced significant deterioration and some Si particles even delaminated from the Cu current collector, consistent with the fast capacity degradation with its long-term cycling performance. Meanwhile, as seen from Fig. S10,† the Si anodes from ethereal samples (the DME13, 1NM313, FDG18 and FDG13 electrolytes) retained bonding with Cu current collectors and no delamination was observed. We hypothesize polymerization of ethereal solvents during long term cycling is responsible for the electrode adhesion to the current collector. Due to the consistent morphological structure for all NMC811 and Si electrodes, interface chemistry between electrodes/electrolyte is expected to be the primary driver of their electrochemical performances.

Thus, to further understand the underlying reasons for the long-term cycling performance of FDG-based electrolytes, we investigated the cathode-electrolyte interphases (CEIs) on the NMC811 cathode and the SEI on the Si anode using X-ray photoelectron spectroscopy (XPS) analysis. The electrodes were rinsed 3 times with battery grade DME solvent to remove residue salts. The full XPS depth profiles (F 1s, C 1s, O 1s, N 1s, Si 2p and S 2p spectra) of NMC811 and Si electrodes experiencing formation and 500 cycling are summarized in Fig. S11–S14.†

For peaks in the C 1s spectra, they originate from the decomposition products of solvent, polyvinylidene fluoride (PVDF) binder, and carbon black. Specifically, these peaks correspond to various chemical species, including C–O–C at 285.7 eV, C–OH at 286.2 eV, C═O at 287.6 eV, O–C═O at 288.2 eV, OCOO at 290.1 eV, and CF_3 at ~293 eV. Additionally, the PVDF binder contributes a CF_2 peak at 290.9 eV, while carbon black exhibits a C–C peak at 284.8 eV. Fig. 6a and b illustrate the C 1 s spectra obtained from the NMC811 cathodes after the formation process (with 2 minutes of sputtering) and after 500 cycles (with 3 minutes of sputtering). To assess the relative stability of the liquid electrolyte, the ratio of decomposition products (C–O–C, C–OH, C═O, O–C═O, OCOO, and

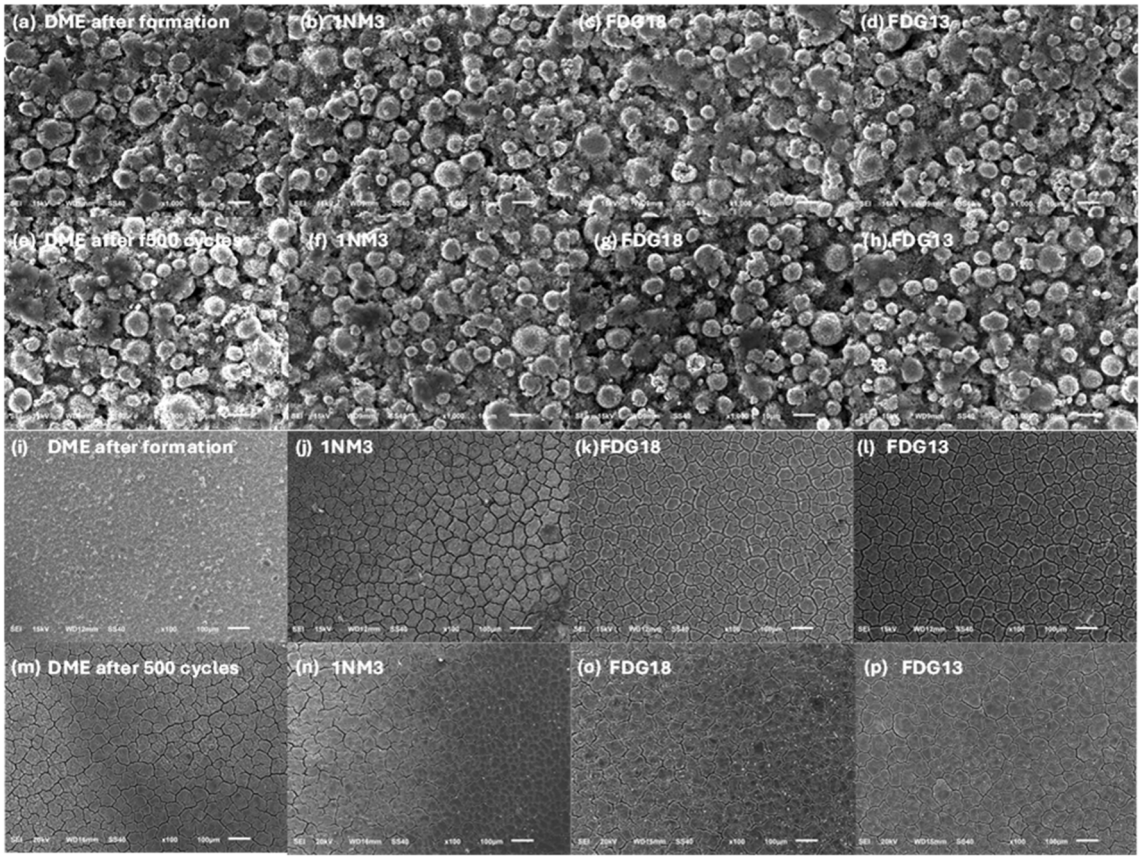

Fig. 5 The evolution of morphologies for electrodes extracted from coin cells (a)–(d) the morphology of NMC811 cathodes after formation; (e)–(h) the morphology of NMC811 cathodes after 500 cycles; (i)–(l) the morphology of Si anodes after the formation; (m)–(p) the morphology of Si anodes after 500 cycles.

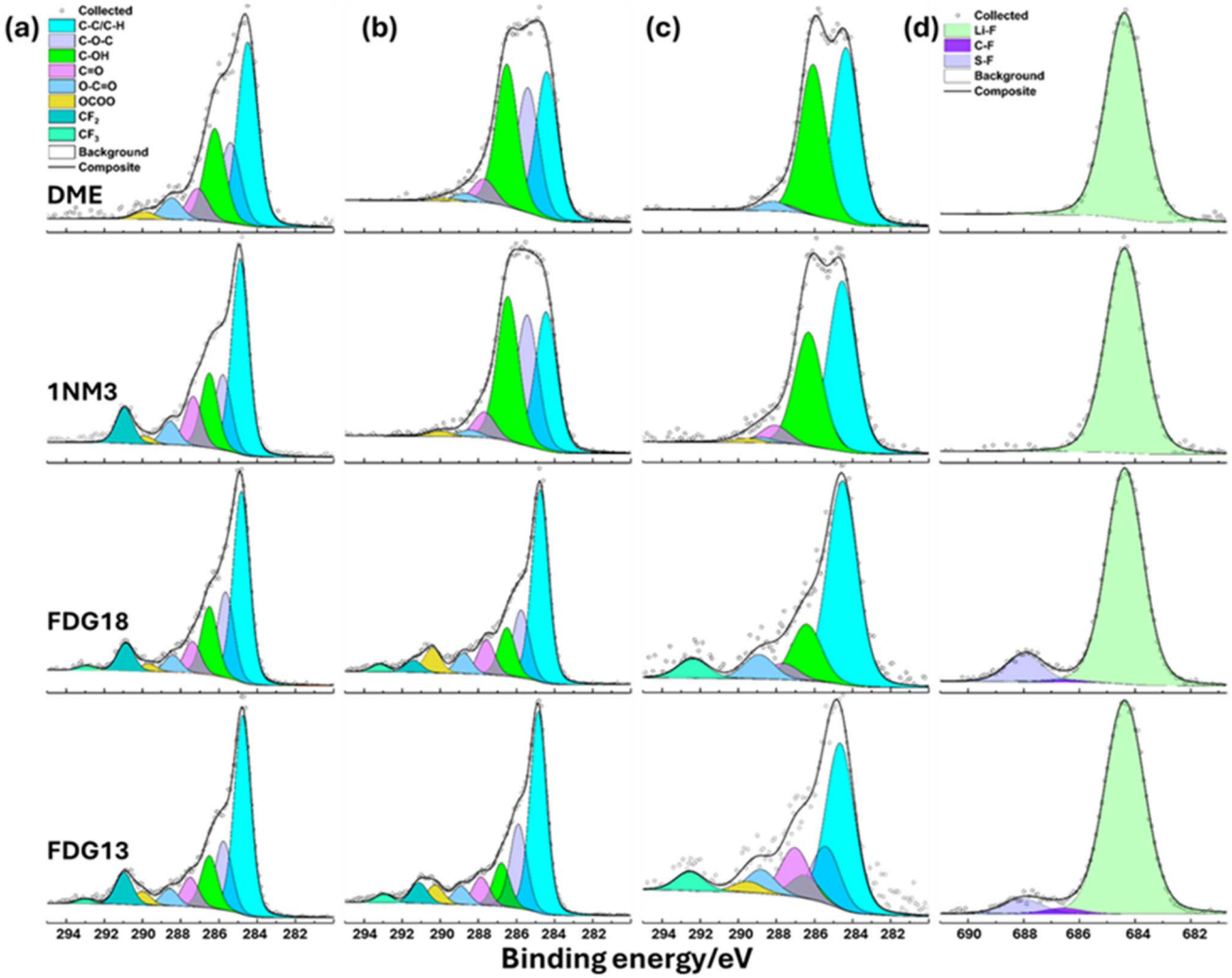

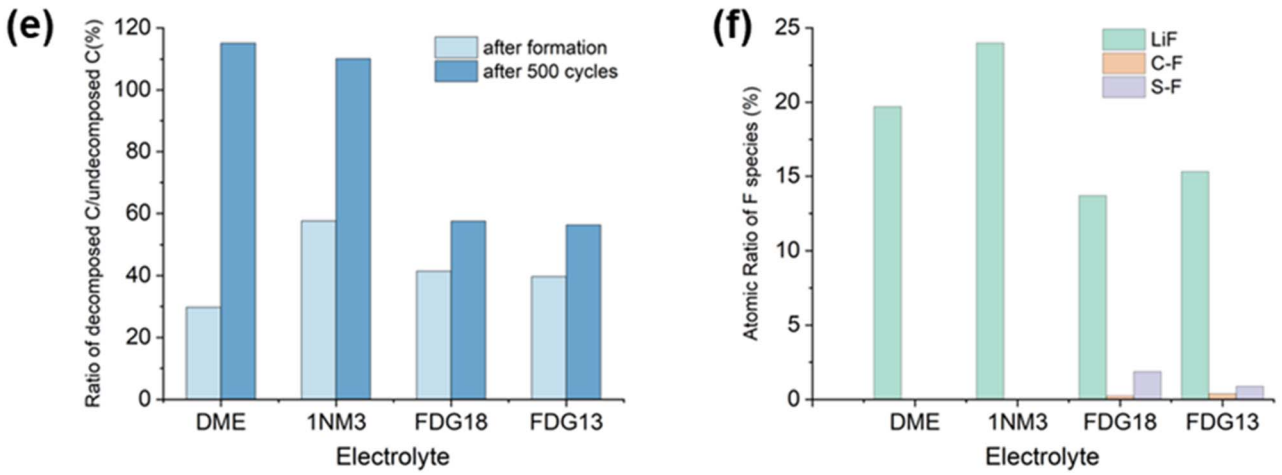

Fig. 6 (a) The C 1s spectra of NMC811 cathode experiencing formation process, with sputtering time of 2 minutes; (b) the C 1s spectra of NMC811 cathodes experiencing 500 cycles, with 3 minutes of sputtering; (c) the C 1s spectra obtained on Si anode after 500 cycles, with 3 minutes of sputtering; (d)The F 1s spectra of Si anode experiencing 500 cycles, with 3 minutes of sputtering; (e) the atomic ratio between decomposed C species and undecomposed C species based on the peak analysis from (a) and (b); (f) the atomic ratio of different F species based on the peak analysis from (d).

CF_3) to non-decomposition products (C–C from carbon black and CF_2 from the PVDF binder) was calculated. A higher ratio indicates greater electrolyte decomposition and lower oxidative stability at the NMC811 cathode.

For the inner cathode-electrolyte interphase (CEI) layers, analyzed after 2 minutes of sputtering, the relative peak ratios from peak deconvolution for four different electrolyte systems are summarized in Table S1,† while the calculated atomic ratios are presented in Fig. 6e. After the formation cycles, the decomposition ratio for the electrolyte system 1NM3 was the highest, followed by FDG18, FDG13, and DME, indicating that the latter three electrolytes exhibit better oxidative stability initially. After 500 cycles, the decomposition ratios for 1NM3 increased significantly, approximately doubling, suggesting continued solvent degradation during extended cycling. In contrast, the FDG18 and FDG13 electrolytes showed only a ~50% increase in their decomposition ratios, demonstrating superior oxidative stability at the NMC811 cathode interface. Notably, the highest decomposition ratio observed for DME highlights substantial electrolyte degradation at the NMC811 interface over prolonged cycling. This observation confirms that ethers, such as unmodified DME, are inherently unstable beyond 4.0 V (*vs.* Li/Li^+) due to their pronounced tendency to decompose under high-voltage conditions in lithium-ion batteries. This severe decomposition is likely to accelerate the dissolution of transition metals, thereby exacerbating the cross-talk effect on Si anodes. Such interactions can contribute to the rapid degradation of electrochemical performance.[42,43]

In addition to the analysis of the CEI formed on NMC811 cathodes, the SEI on Si anodes was also examined using XPS depth profiling. The C 1s spectra for Si anodes after 500 cycles (with 3 minutes of sputtering) are summarized in Fig. 6c. The peak assignments follow the same pattern as those for the C 1s spectra from the NMC811 electrodes. By analyzing the area ratio of decomposition products to the C–C peak from carbon black, insights into the extent of electrolyte decomposition can also be gained. As shown in Table S2,† the ratios for FDG18 and FDG13 electrolytes are significantly lower than those for the DME and 1NM3-based electrolytes, indicating slower decomposition of FDG-based electrolytes on the Si anodes.

For the F 1s spectra shown in Fig. 6d, it consists of Li–F (684.7 eV) from LiF, C–F (687 eV) from the FDG solvent, and S–F (688 eV) from the decomposition products of FSI anions. For DME- and 1NM3-based electrolytes, the SEI is composed exclusively of LiF (Fig. 6d and f), indicating complete defluorination of the FSI^- anion. In contrast, for FDG-based electrolytes, the SEI contains LiF, C–F from interaction with FDG, and S–F, although the latter two components exhibit relatively low atomic ratios. This suggests that after the formation of LiF as the primary product, the remaining $FSO_2NSO_2^{2-}$ species undergoes further decomposition upon the addition of $2e^-$ from the Si electrode, yielding SO_2^{2-} and $NFSO_2^{2-}$ as secondary decomposition products. This mechanism highlights the distinct defluorination pathways and decomposition behavior of FSI^- anions in FDG-based electrolytes compared to DME- and 1NM3-based systems. The presence of organofluoride species (C–F) from fluorinated solvents like FDG, alongside inorganic components such as LiF, may enhance the chemical and mechanical stability of the SEI by resisting further decomposition and improving ion transport, as reflected in the total F atomic concentration shown in Fig. S15a.† After 500 cycles, the atomic concentration of fluorine in the SEI layers on Si anodes reveals distinct trends: DME13 exhibits the highest F content (24.1% in the innermost layer), followed by 1NM313 (19.7%), while FDG-based electrolytes (FDG18 and FDG13) show significantly lower F concentrations (15.8% and 16.6%, respectively). The high F concentration in DME13 indicates extensive LiFSI decomposition and poor electrolyte stability, whereas the lower F content in FDG-based electrolytes suggests improved stability due to the formation of an initial SEI layer that prevents further salt decomposition and stabilizes the system during extended cycling. This highlights the ability of FDG-based electrolytes to promote a robust and protective SEI, enhancing overall stability on Si anodes. However, the role of organofluoride species in SEI formation, structure, and long-term performance remains unclear. Further investigation into their formation mechanism, distribution, and electrochemical behavior could provide valuable insights for future optimizing electrolyte formulations to improve battery performance and stability. The enhanced stability of FDG-based electrolytes is closely tied to their solvation structure. While free FSI^- anions are more prone to decomposition, FDG-based electrolytes exhibit higher levels of AGGs and coordinated FSI^- anions which reduces the likelihood of FSI^- decomposition, thereby improving the reductive stability of FDG-based electrolytes at the Si anode interface. On the other hand, while we recognize the essential role of fluorinated compounds in current lithium-ion battery technology, we emphasize the need for effective recycling programs to mitigate their environmental impact. Additionally, the use of non-fluorinated co-solvents, such as ionic liquids and anisole, presents a promising strategy to reduce the hazards associated with solvents containing $–CF_3$ and/or $–CF_2–$ groups but maintaining its performance in the future.[44]

Furthermore, as shown in Fig. S15b,† the atomic concentration of silicon (Si) in each SEI layer (measured at sputtering times of 0, 1, 2, and 3 minutes) is significantly higher for samples using FDG18 and FDG13 electrolytes. This trend is further supported by the Si 2p spectra (after 3 minutes of sputtering) of Si anodes after 500 cycles, as summarized in Fig. S15c.† The Si 2p spectra predominantly feature Li_xSiO_y (~101 eV) and Li_xSi (~97 eV), both of which are typical components of the inner SEI on Si anodes. Interestingly, Si anodes from FDG18 and FDG13 electrolytes exhibit substantially higher Li_xSi content than those from DME and 1NM313 electrolytes: 40.5% Li_xSi for FDG13 sample, 40.14% Li_xSi for FDG18 sample, 22.3% Li_xSi for 1NM3 sample and 26.06% for DME sample. The notably higher Li_xSi content in FDG-based electrolytes suggests a potential correlation between Li_xSi formation in SEI and electrochemical performance. Previous studies by Zhang *et al.* indicate that complex interactions exist between SEI and Li_xSi, where Li_xSi can be either active or inactive, depending on the specific electrolyte composition.[45–47] Here, the linkage between Li_xSi contents and overall performance remains elusive and it will be probed in our future work.

3 Conclusion

In this study we proposed the idea to tune the oxidation and solvation properties of ethereal solvents *via* molecular engineering, to realize their application in NMC811||Si full cells. The trimethylsilane and terminal $-CF_3$ functional groups were proposed and the obtained 1NM3 and FDG solvents were evaluated. Compared to commonly used ethereal solvents like DME and DG, obtained 1NM3 and FDG solvents indeed exhibit improved oxidative stability at the cathode side. This is well confirmed by their enhanced HOMO levels *via* DFT calculations and the decreased leaking current *via* potentiostatic holding experiment. Meanwhile, obtained solvents exhibited weakened solvation capability, leading to the formation of more AGGs within the liquid electrolyte. Correspondingly, more FSI anions participate into the interfacial composition. This enables beneficial interfacial chemistry stability for the Si anode. The improved oxidative stability and beneficial SEIs formed from AGGs lead to less side reactions between electrode and liquid electrolyte, contributing together to the superb long-term cycling performances for Si||NMC811 full cells. Thus, this molecular engineering strategy verifies its rationality and shed further light to the design and development of novel electrolytes for LIBs.

4 Experimental

4.1 Materials

The chemical structures of the tested ethereal solvents (DME, DG, 1NM3, FDG) and the LiFSI salt are summarized in Scheme 1. The ethereal solvents, 1NM3 (from MERF Facility, Argonne National Laboratory), DG (Gotion), DME (Gotion) were dehydrated using 4 Å molecular sieves and then vacuum distilled before use. The synthesis scheme of FDG was schematically shown in Scheme 2. Under nitrogen atmosphere, 2,2,2-trifluoroethanol was first added into the mixture of sodium hydride and tetrahydrofuran (THF). After stirring the mixture, oxybis(ethane-2.1-diyl)bis (4-methylbenzenesulfonate) dissolved in THF was added into the fluoroalkoxide solution at 0 °C. The resulting solution was then quenched *via* water. Then, the reaction mixture was extracted *via* ethyl acetate and then dried *via* anhydrous sodium sulfate. After removing the solvent *via* rotary evaporator, the product was further dried *via* molecular sieves and purified *via* vacuum distillation. More detailed synthesis information for the FDG solvent can be found in our previous publication.[20] Comparing the Fourier-transform infrared spectroscopy (FTIR) spectra of DG and FDG solvents shown in Fig. S1,† the absorption modes from the added $-CF_3$ functional group can be well seen between 665 cm^{-1} and 1275 cm^{-1}.

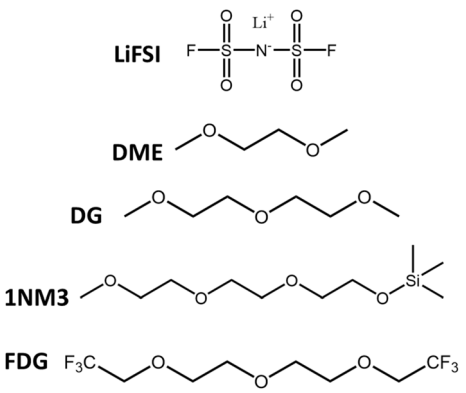

Scheme 1 Chemical structures of LiFSI salt and the other 4 ethereal solvents (DME, DG, 1NM3, FDG) probed in this study.

4.2 Electrochemical testing

The detailed formulations of tested electrolyte systems are summarized in Table 1. For the long-term cycling performance, both the NMC811 cathodes and Si anodes were obtained from Cell Analysis, Modeling, and Prototyping (CAMP) Facility at Argonne National Laboratory. The detailed information on these electrode materials was summarized in Table 2. For the preparation of nano-sized Si powders, it was prepared from intrinsic silicon boules from EI-Cat and the detailed preparation process can be found in the reference paper.[48] The crystal structure of milled Si nano powers was probed *via* XRD and the morphology of prepared Si anode was further probed *via* SEM, and the results were also summarized in Fig. S2.†

For the long-term cycling, the NMC811||Si full cells (with diameters of 14 mm for NMC811 and 15 mm for Si anode) filled with these 5 electrolyte systems were prepared in glovebox filled with Ar gas. The O_2 and H_2O content within the glovebox is less than 1 ppm. The separator was Celgard 2325. For the prepared coin cells, 40 μl electrolyte was used and the Al-deposited coin base was utilized to prevent possible Al corrosion from LiFSI salt during cycling.[49] For the measurement of ion conductivity for all tested electrolytes, it is implemented *via* coin cell, and the detailed cell configuration was shown in Fig. S3.†[50]

4.2.1 FTIR. Fourier-transform infrared spectroscopy (FTIR) was utilized to probe the solvation structure of these electrolyte systems. An attenuated total reflection (ATR) Alpha FT-IR spectrometer from PerkinElmer, with a diamond crystal as refractive element and placed inside the glove box, was used to record the IR spectra using 1 scan for the samples and 3 scans for the background. Data was collected at 30 °C between 400 and 4000 cm^{-1} with a resolution of 2 cm^{-1}.

4.2.2 DFT calculation. The highest occupied molecular orbital (HOMO) and lowest unoccupied molecular orbital (LUMO) levels of the four solvent molecules were calculated using Gaussian 16 simulation package. The structures were pre-optimized using B3LYP hybrid functional and the triple-zeta

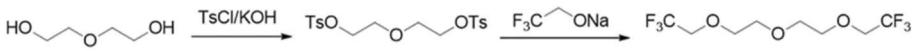

Scheme 2 The synthesis procedure of FDG ether used in this study.

Table 2 Detailed components for the electrodes utilized in this study

	Cathode	Si anode
Composition	NMC811	Si
Active material	90 wt% Targray NMC811	80 wt% Si
Binder	5 wt% Solvay 530 poly(vinylidene fluoride) (PVDF)	10 wt% P84 polyimide by Ensinger
Conducting agent	5 wt% Timcal C45 carbon	10 wt% Timcal C45 carbon
Loading density (mg cm^{-2})	15.81	1.19
Coating thickness (μm)	59	14
Areal capacity (mA h cm^{-2})	2.59	2.07
Porosity	34.5%	57.2%

basis set 6-311+G*.[51–56] Then MP2 method was adopted to investigate the electronic structures.[57,58] The SMD solvation model was applied; the dielectric constant for DME, DG, 1NM3, and FDG are 7.2, 5.7, 5.13, and 7.3, respectively.[59]

4.2.3 SEM. All micrographs were collected on a JEOL600 scanning electron microscope. Generally, with the accelerating voltages ranged between 10 and 20 kV and the pressure <10 e^{-4} mBar. All samples that had undergone XPS analysis were subsequently subjected to SEM analysis. Samples were moved between the SEM and the XPS in an inert environment after careful observation of the study positions.

4.2.4 XPS characterization. XPS data for cells experiencing formation and long-term cycling were acquired using PHI 5000 VersaProbe II system (Physical Electronics) attached to an argon-atmosphere glovebox. The base pressure was $\sim 1 \times 10^{-8}$ Torr. The prepared samples were placed in the XPS chamber by moving them through the glovebox (no air exposure). The spectra were obtained under the following conditions: 100 μm beam (25 W) with Al Kα radiation ($h\nu = 1486.6$ eV), Ar^+-ion and electron beam sample neutralization, fixed analyzer transmission mode, and pass energy of 23.50 eV. The Shirly background data were subtracted from all spectra. The spectra were fitted to multiple Gaussian peaks by using the software package (Multipack) that Physical Electronics provided. The XPS spectra was calibrated onto the C–C bond at 284.8 ev. The concentrations are the average of data collected from three locations. Depth profiling was performed using monatomic Ar^+ sputtering at 1.0 keV every 1 min for 3 cycles over a 3×3 mm^2 raster area.

4.2.5 NMR characterization. NMR spectra for synthesized FDG solvents were implemented on Bruker spectrometer at 300 MHz. For the ^1H chemical shifts, it was referenced at 7.27 ppm of chloroform-d ($CDCl_3$).

Data availability

The data that support the findings of this study are available from the corresponding author upon reasonable request.

Author contributions

Xianyang Wu and Chi-Cheung Su contributed equally to this work. Wu X.: conceptualization, investigation, methodology, formal analysis, and writing of the manuscript; Su C.: conceptualization, investigation, methodology, formal analysis, and writing of the manuscript; Li X.: investigation and resources; Xu, J.: investigation; Amine K.: review and editing; Wu D.: investigation and resources; Li T.: investigation and resources; Yang Z.: conceptualization (lead), investigation (lead), methodology, formal analysis, and writing of the manuscript; Ingram B.: supervision, review and editing, funding acquisition and project administration. All authors have given approval to the final version of the manuscript.

Conflicts of interest

There are no conflicts to declare.

Acknowledgements

Research at Argonne National Laboratory was supported by the U.S. Department of Energy (DOE), Office of Energy Efficiency and Renewable Energy, Vehicle Technologies Office under the Silicon Consortium project. Argonne National Laboratory is operated for the DOE Office of Science by UChicago Argonne, LLC, under Contract DE-AC02-06CH11357. The electrodes used in this article were made by Argonne's Cell Analysis, Modeling and Prototyping (CAMP) Facility, which was supported by the Applied Battery Research for Transportation Program.

References

1 T. Nagaura, *Development of Rechargeable Lithium Batteries*, JRC Battery Newsletter, 1991, pp. 10–18.
2 X. Zeng, M. Li, D. Abd El-Hady, W. Alshitari, A. S. Al-Bogami, J. Lu and K. Amine, Commercialization of Lithium Battery Technologies for Electric Vehicles, *Adv. Energy Mater.*, 2019, **9**(27), 1900161.
3 M. B. Armand, Intercalation Electrodes, in *Materials for Advanced Batteries*, ed. Murphy, D. W., Broadhead, J. and Steele, B. C. H., Springer US, Boston, MA, 1980; pp pp 145–161.
4 J. R. Dahn, T. Zheng, Y. Liu and J. S. Xue, Mechanisms for Lithium Insertion in Carbonaceous Materials, *Science*, 1995, **270**(5236), 590–593.
5 H. Zhang, Y. Yang, D. Ren, L. Wang and X. He, Graphite as anode materials: Fundamental mechanism, recent progress and advances, *Energy Storage Mater.*, 2021, **36**, 147–170.

6 J. Neubauer and E. Wood, The impact of range anxiety and home, workplace, and public charging infrastructure on simulated battery electric vehicle lifetime utility, *J. Power Sources*, 2014, **257**, 12–20.
7 M. N. Obrovac and L. Christensen, Structural Changes in Silicon Anodes during Lithium Insertion/Extraction, *Electrochem. Solid-State Lett.*, 2004, **7**(5), A93.
8 M. N. Obrovac and V. L. Chevrier, Alloy Negative Electrodes for Li-Ion Batteries, *Chem. Rev.*, 2014, **114**(23), 11444–11502.
9 M. Ko, S. Chae and J. Cho, Challenges in Accommodating Volume Change of Si Anodes for Li-Ion Batteries, *ChemElectroChem*, 2015, **2**(11), 1645–1651.
10 S. Chae, M. Ko, K. Kim, K. Ahn and J. Cho, Confronting Issues of the Practical Implementation of Si Anode in High-Energy Lithium-Ion Batteries, *Joule*, 2017, **1**(1), 47–60.
11 J. D. McBrayer, M.-T. F. Rodrigues, M. C. Schulze, D. P. Abraham, C. A. Apblett, I. Bloom, G. M. Carroll, A. M. Colclasure, C. Fang, K. L. Harrison, G. Liu, S. D. Minteer, N. R. Neale, G. M. Veith, C. S. Johnson, J. T. Vaughey, A. K. Burrell and B. Cunningham, Calendar aging of silicon-containing batteries, *Nat. Energy*, 2021, **6**(9), 866–872.
12 D. Schneier, Y. Shaham, G. Ardel, L. Burstein, Y. Kamir and E. Peled, Elucidation of the Spontaneous Passivation of Silicon Anodes in Lithium Battery Electrolytes, *J. Electrochem. Soc.*, 2019, **166**(16), A4020.
13 K. Guo, R. Kumar, X. Xiao, B. W. Sheldon and H. Gao, Failure progression in the solid electrolyte interphase (SEI) on silicon electrodes, *Nano Energy*, 2020, **68**, 104257.
14 G. Yang, S. Frisco, R. Tao, N. Philip, T. H. Bennett, C. Stetson, J.-G. Zhang, S.-D. Han, G. Teeter, S. P. Harvey, Y. Zhang, G. M. Veith and J. Nanda, Robust Solid/Electrolyte Interphase (SEI) Formation on Si Anodes Using Glyme-Based Electrolytes, *ACS Energy Lett.*, 2021, **6**(5), 1684–1693.
15 T. T. Beyene, H. K. Bezabh, M. A. Weret, T. M. Hagos, C.-J. Huang, C.-H. Wang, W.-N. Su, H. Dai and B.-J. Hwang, Concentrated Dual-Salt Electrolyte to Stabilize Li Metal and Increase Cycle Life of Anode Free Li-Metal Batteries, *J. Electrochem. Soc.*, 2019, **166**(8), A1501.
16 J. Yang, X. Li, K. Qu, Y. Wang, K. Shen, C. Jiang, B. Yu, P. Luo, Z. Li, M. Chen, B. Guo, M. Wang, J. Chen, Z. Ma, Y. Huang, Z. Yang, P. Liu, R. Huang, X. Ren and D. Mitlin, Concentrated ternary ether electrolyte allows for stable cycling of a lithium metal battery with commercial mass loading high-nickel NMC and thin anodes, *Carbon Energy*, 2023, **5**(3), e275.
17 Z. Zhang, J. Lu, R. S. Assary, P. Du, H.-H. Wang, Y.-K. Sun, Y. Qin, K. C. Lau, J. Greeley, P. C. Redfern, H. Iddir, L. A. Curtiss and K. Amine, Increased Stability Toward Oxygen Reduction Products for Lithium-Air Batteries with Oligoether-Functionalized Silane Electrolytes, *J. Phys. Chem. C*, 2011, **115**(51), 25535–25542.
18 B. Philippe, R. Dedryvère, M. Gorgoi, H. Rensmo, D. Gonbeau and K. Edström, Improved Performances of Nanosilicon Electrodes Using the Salt LiFSI: A Photoelectron Spectroscopy Study, *J. Am. Chem. Soc.*, 2013, **135**(26), 9829–9842.
19 L. Lv, Y. Wang, W. Huang, Y. Wang, G. Zhu and H. Zheng, Effect of lithium salt type on silicon anode for lithium-ion batteries, *Electrochim. Acta*, 2022, **413**, 140159.
20 C.-C. Su, J. Shi, R. Amine, M. He, S.-B. Son, J. Guo, M. Jiang and K. Amine, Terminally fluorinated glycol ether electrolyte for lithium metal batteries, *Nano Energy*, 2023, **110**, 108335.
21 O. Borodin, X. Ren, J. Vatamanu, A. von Wald Cresce, J. Knap and K. Xu, Modeling Insight into Battery Electrolyte Electrochemical Stability and Interfacial Structure, *Acc. Chem. Res.*, 2017, **50**(12), 2886–2894.
22 P. Peljo and H. H. Girault, Electrochemical potential window of battery electrolytes: the HOMO–LUMO misconception, *Energy Environ. Sci.*, 2018, **11**(9), 2306–2309.
23 Z. Yu, P. E. Rudnicki, Z. Zhang, Z. Huang, H. Celik, S. T. Oyakhire, Y. Chen, X. Kong, S. C. Kim, X. Xiao, H. Wang, Y. Zheng, G. A. Kamat, M. S. Kim, S. F. Bent, J. Qin, Y. Cui and Z. Bao, Rational solvent molecule tuning for high-performance lithium metal battery electrolytes, *Nat. Energy*, 2022, **7**(1), 94–106.
24 Y. Lin, Z. Yu, W. Yu, S.-L. Liao, E. Zhang, X. Guo, Z. Huang, Y. Chen, J. Qin, Y. Cui and Z. Bao, Impact of the fluorination degree of ether-based electrolyte solvents on Li-metal battery performance, *J. Mater. Chem. A*, 2024, **12**(5), 2986–2993.
25 C. Xu, F. Lindgren, B. Philippe, M. Gorgoi, F. Björefors, K. Edström and T. Gustafsson, Improved Performance of the Silicon Anode for Li-Ion Batteries: Understanding the Surface Modification Mechanism of Fluoroethylene Carbonate as an Effective Electrolyte Additive, *Chem. Mater.*, 2015, **27**(7), 2591–2599.
26 V. Etacheri, O. Haik, Y. Goffer, G. A. Roberts, I. C. Stefan, R. Fasching and D. Aurbach, Effect of Fluoroethylene Carbonate (FEC) on the Performance and Surface Chemistry of Si-Nanowire Li-Ion Battery Anodes, *Langmuir*, 2012, **28**(1), 965–976.
27 Y. Jin, N.-J. H. Kneusels, L. E. Marbella, E. Castillo-Martínez, P. C. M. M. Magusin, R. S. Weatherup, E. Jónsson, T. Liu, S. Paul and C. P. Grey, Understanding Fluoroethylene Carbonate and Vinylene Carbonate Based Electrolytes for Si Anodes in Lithium Ion Batteries with NMR Spectroscopy, *J. Am. Chem. Soc.*, 2018, **140**(31), 9854–9867.
28 Y. Zhao, T. Zhou, M. Mensi, J. W. Choi and A. Coskun, Electrolyte engineering *via* ether solvent fluorination for developing stable non-aqueous lithium metal batteries, *Nat. Commun.*, 2023, **14**(1), 299.
29 K. Xu, "Charge-Transfer" Process at Graphite/Electrolyte Interface and the Solvation Sheath Structure of Li^+ in Nonaqueous Electrolytes, *J. Electrochem. Soc.*, 2007, **154**(3), A162.
30 A. von Wald Cresce, O. Borodin and K. Xu, Correlating Li^+ Solvation Sheath Structure with Interphasial Chemistry on Graphite, *J. Phys. Chem. C*, 2012, **116**(50), 26111–26117.
31 J. Zheng, J. A. Lochala, A. Kwok, Z. D. Deng and J. Xiao, Research Progress towards Understanding the Unique Interfaces between Concentrated Electrolytes and Electrodes for Energy Storage Applications, *Advanced Science*, 2017, **4**(8), 1700032.

32 D. M. Seo, S. Reininger, M. Kutcher, K. Redmond, W. B. Euler and B. L. Lucht, Role of Mixed Solvation and Ion Pairing in the Solution Structure of Lithium Ion Battery Electrolytes, *J. Phys. Chem. C*, 2015, **119**(25), 14038–14046.

33 T. Hou, K. D. Fong, J. Wang and K. A. Persson, The solvation structure, transport properties and reduction behavior of carbonate-based electrolytes of lithium-ion batteries, *Chem. Sci.*, 2021, **12**(44), 14740–14751.

34 M. Kerner, N. Plylahan, J. Scheers and P. Johansson, Thermal stability and decomposition of lithium bis(fluorosulfonyl)imide (LiFSI) salts, *RSC Adv.*, 2016, **6**(28), 23327–23334.

35 M. Beran, J. Příhoda, Z. Žák and M. Černík, A new route to the syntheses of alkali metal bis(fluorosulfuryl)imides: crystal structure of $LiN(SO_2F)_2$, *Polyhedron*, 2006, **25**(6), 1292–1298.

36 J. Huang and A. F. Hollenkamp, Thermal Behavior of Ionic Liquids Containing the FSI Anion and the Li^+ Cation, *J. Phys. Chem. C*, 2010, **114**(49), 21840–21847.

37 A. Gabryelczyk, S. Ivanov, A. Bund and G. Lota, Corrosion of aluminium current collector in lithium-ion batteries: a review, *J. Energy Storage*, 2021, **43**, 103226.

38 S. S. Zhang and T. R. Jow, Aluminum corrosion in electrolyte of Li-ion battery, *J. Power Sources*, 2002, **109**(2), 458–464.

39 S. Ko, T. Obukata, T. Shimada, N. Takenaka, M. Nakayama, A. Yamada and Y. Yamada, Electrode potential influences the reversibility of lithium-metal anodes, *Nat. Energy*, 2022, **7**(12), 1217–1224.

40 P. C. Knutson, A. J. Teator, T. P. Varner, C. T. Kozuszek, P. E. Jacky and F. A. Leibfarth, Brønsted Acid Catalyzed Stereoselective Polymerization of Vinyl Ethers, *J. Am. Chem. Soc.*, 2021, **143**(40), 16388–16393.

41 S. Pidaparthy, M. Luo, M.-T. F. Rodrigues, J.-M. Zuo and D. P. Abraham, Physicochemical Heterogeneity in Silicon Anodes from Cycled Lithium-Ion Cells, *ACS Appl. Mater. Interfaces*, 2022, **14**(34), 38660–38668.

42 O. C. Harris, S. E. Lee, C. Lees and M. Tang, Review: mechanisms and consequences of chemical cross-talk in advanced Li-ion batteries, *J. Phys.: Energy*, 2020, **2**(3), 032002.

43 M. Kim, Z. Yang, S.-B. Son, S. E. Trask, A. Jansen and I. Bloom, Effect of cathode on crosstalk in Si-based lithium-ion cells, *J. Mater. Chem. A*, 2021, **9**(47), 26904–26916.

44 X. Liu, A. Mariani, T. Diemant, M. E. Di Pietro, X. Dong, P.-H. Su, A. Mele and S. Passerini, PFAS-Free Locally Concentrated Ionic Liquid Electrolytes for Lithium Metal Batteries, *ACS Energy Lett.*, 2024, **9**(6), 3049–3057.

45 X. Zhang, S. Weng, G. Yang, Y. Li, H. Li, D. Su, L. Gu, Z. Wang, X. Wang and L. Chen, Interplay between solid-electrolyte interphase and (in)active LixSi in silicon anode, *Cell Rep. Phys. Sci.*, 2021, **2**(12), 100668.

46 Z. Yang, X. Qin, K. Lin, Q. Cai, Y. Fu and B. Li, Surface passivated LixSi with improved storage stability as a prelithiation reagent in anodes, *Electrochem. Commun.*, 2022, **138**, 107272.

47 E. Wang, M.-T. F. Rodrigues, S. Park, F. Dogan and B. Key, Operando NMR characterization of cycled and calendar aged nanoparticulate silicon anodes for Li-ion batteries, *J. Power Sources*, 2024, **604**, 234477.

48 J. Cai, X. Zhou, T. Li, H. T. Nguyen, G. M. Veith, Y. Qin, W. Lu, S. E. Trask, M.-T. Fonseca Rodrigues, Y. Liu, W. Xu, M. C. Schulze, A. K. Burrell and Z. Chen, Critical Contribution of Imbalanced Charge Loss to Performance Deterioration of Si-Based Lithium-Ion Cells during Calendar Aging, *ACS Appl. Mater. Interfaces*, 2023, **15**(41), 48085–48095.

49 S. Chen, J. Zheng, L. Yu, X. Ren, M. H. Engelhard, C. Niu, H. Lee, W. Xu, J. Xiao, J. Liu and J.-G. Zhang, High-Efficiency Lithium Metal Batteries with Fire-Retardant Electrolytes, *Joule*, 2018, **2**(8), 1548–1558.

50 Z. Yu, W. Yu, Y. Chen, L. Mondonico, X. Xiao, Y. Zheng, F. Liu, S. T. Hung, Y. Cui and Z. Bao, Tuning Fluorination of Linear Carbonate for Lithium-Ion Batteries, *J. Electrochem. Soc.*, 2022, **169**(4), 040555.

51 A. D. Becke, Density-functional thermochemistry. III. The role of exact exchange, *J. Chem. Phys.*, 1993, **98**(7), 5648–5652.

52 C. Lee, W. Yang and R. G. Parr, Development of the Colle-Salvetti correlation-energy formula into a functional of the electron density, *Phys. Rev. B:Condens. Matter Mater. Phys.*, 1988, **37**(2), 785–789.

53 S. H. Vosko, L. Wilk and M. Nusair, Accurate spin-dependent electron liquid correlation energies for local spin density calculations: a critical analysis, *Can. J. Phys.*, 1980, **58**(8), 1200–1211.

54 P. J. Stephens, F. J. Devlin, C. F. Chabalowski and M. J. Frisch, Ab Initio Calculation of Vibrational Absorption and Circular Dichroism Spectra Using Density Functional Force Fields, *J. Phys. Chem.*, 1994, **98**(45), 11623–11627.

55 A. D. McLean and G. S. Chandler, Contracted Gaussian basis sets for molecular calculations. I. Second row atoms, $Z = 11$–18, *J. Chem. Phys.*, 1980, **72**(10), 5639–5648.

56 R. Krishnan, J. S. Binkley, R. Seeger and J. A. Pople, Self-consistent molecular orbital methods. XX. A basis set for correlated wave functions, *J. Chem. Phys.*, 1980, **72**(1), 650–654.

57 M. J. Frisch, M. Head-Gordon and J. A. Pople, Semi-direct algorithms for the MP2 energy and gradient, *Chem. Phys. Lett.*, 1990, **166**(3), 281–289.

58 M. Head-Gordon, J. A. Pople and M. J. Frisch, MP2 energy evaluation by direct methods, *Chem. Phys. Lett.*, 1988, **153**(6), 503–506.

59 A. V. Marenich, C. J. Cramer and D. G. Truhlar, Universal Solvation Model Based on Solute Electron Density and on a Continuum Model of the Solvent Defined by the Bulk Dielectric Constant and Atomic Surface Tensions, *J. Phys. Chem. B*, 2009, **113**(18), 6378–6396.